Thermoelectric properties of the As/P-based Zintl compounds $EuIn_2As_{2-x}P_x$ ($x = 0$ to 2) and $SrSn_2As_2$

Keisuke Shinozaki,[1] Yosuke Goto,[1,*] Kazuhisa Hoshi,[1] Ryosuke Kiyama,[1] Naoto Nakamura,[1] Akira Miura,[2] Chikako Moriyoshi,[3] Yoshihiro Kuroiwa,[3] Hidetomo Usui,[4,*] Yoshikazu Mizuguchi[1]

[1]Department of Physics, Tokyo Metropolitan University, 1-1 Minami-osawa, Hachioji, Tokyo 192-0397, Japan

[2]Faculty of Engineering, Hokkaido University, Kita 13, Nishi 8 Sapporo 060-8628, Japan

[3]Graduate School of Advanced Science and Engineering, Hiroshima University, 1-3-1 Kagamiyama, Higashihiroshima, Hiroshima 739-8526, Japan

[4]Department of Physics and Materials Science, Shimane University, Matsue, 690-8504, Japan

e-mail: y_goto@tmu.ac.jp, hidetomo.usui@riko.shimane-u.ac.jp

Abstract

Zintl compounds containing Sb have been studied extensively because of their promising thermoelectric properties. In this study, we prepared As/P-based Zintl compounds, $EuIn_2As_{2-x}P_x$ ($x = 0$ to 2) and $SrSn_2As_2$, and examined their potential for use as thermoelectric materials. These compounds show p-type polarity with Hall carrier concentrations of $\sim 10^{19}$ cm^{-3} for $EuIn_2As_{2-x}P_x$ and $\sim 10^{21}$ cm^{-3} for $SrSn_2As_2$ at 300 K. The high carrier concentration of $SrSn_2As_2$ is likely owing to self-doping by hole-donating Sn vacancies. The electrical power factor reaches ~ 1 mW m^{-1} K^{-2} at ~ 600 K for $EuIn_2As_{2-x}P_x$ with $x = 0.1$ and 0.2, which is almost twice that of the end-member compounds ($x = 0$ and 2). The lattice thermal conductivity κ_1 is determined to be 1.6–2.0 W m^{-1} K^{-1} for $EuIn_2As_2$ and $SrSn_2As_2$ and 2.8 W m^{-1} K^{-1} for $EuIn_2P_2$ at 673 K. The dimensionless figure of merit reaches $ZT = 0.29$ at 773 K for $EuIn_2As_{2-x}P_x$ with $x = 0.2$ owing to the optimized carrier concentration and/or electronic structure, as well as a reduced lattice thermal conductivity in the solid solution. First-principles calculations show that $EuIn_2As_2$ and $SrSn_2As_2$ are topologically nontrivial materials with band inversion, while $EuIn_2P_2$ is a conventional semiconductor with a bandgap. The present study demonstrates that As/P-based Zintl compounds can also show promising thermoelectric properties, thus expanding the frontier for efficient thermoelectric materials.

Introduction

Thermoelectric devices enable the interconversion between temperature difference and electricity without rotating parts or gas emissions. Consequently, they may provide a means to generate electricity from waste heat or pump heat using electricity. The efficiency of a thermoelectric device is primarily determined by the Carnot efficiency and the material's dimensionless figure of merit, $ZT = S^2 T \rho^{-1} \kappa^{-1}$, where T is the absolute temperature, S is the Seebeck coefficient, ρ is the electrical resistivity, and κ is the thermal conductivity.[1-4] The development of materials that exhibit high values of ZT is desired for efficient thermoelectric conversion; however, this is a difficult task because the transport properties of these materials generally exhibit conflicting dependencies on, for example, the carrier concentration.

Various thermoelectric materials have been investigated for the past several decades. Among them, Zintl compounds, which consist of covalently bonded anionic frameworks and cations, have been studied extensively because of their fascinating compositional/structural varieties and promising thermoelectric properties.[5-7] For example, AB_2X_2, $A_{14}BX_{11}$, A_3BX_3, $A_5B_2X_6$, $A_9B_{4+\delta}X_9$, and A_2BX_2—where A denotes an alkali/alkaline-earth/rare-earth metal, B is a (post-) transition metal, and X is a pnictogen—have been demonstrated as promising thermoelectric materials.[8-15] In particular, $Mg_3(Sb,Bi)_2$—which is also categorized as an AB_2X_2 system because the Mg atoms are located at two crystallographic sites—exhibits $ZT = 1.51$ at 716 K.[13,14] So far, most studies of Zintl thermoelectric compounds have employed Sb as the constituent pnictogen X, while investigations that employ lighter pnictogens such as As and P are still sporadic and not firmly established.[16,17] However, recent studies have demonstrated that As-based Zintl compounds, including $(Ba, K)Zn_2As_2$ and $(Ba, K)Cd_2As_2$, can also show

promising thermoelectric properties.[18-20] Furthermore, *n*-type polarity was unexpectedly observed in Eu_3InAs_3.[21] Although the use of arsenides is not straightforward for practical applications, expanding the frontier for efficient thermoelectric materials may provide a new paradigm for developing next-generation energy materials, as exemplified by iron-arsenide superconductors with high transition temperatures.[22]

Crystal structures of Zintl compounds $EuIn_2As(P)_2$ and $SrSn_2As_2$ belong to the space groups $P6_3/mmc$ for $EuIn_2As(P)_2$ and $R\overline{3}m$ for $SrSn_2As_2$, as shown schematically in Figure 1.[23-25] $EuIn_2As(P)_2$ are attractive because of negative colossal magnetoresistance at around magnetic transition temperature (16 K for $EuIn_2As_2$ and 24 K for $EuIn_2P_2$).[23,24] $EuIn_2As_2$ and $SrSn_2As_2$ have also attracted considerable attention as topological materials.[26-29] Interestingly, topologically nontrivial electronic states and efficient thermoelectric properties are often observed in similar materials, such as $(Bi,Sb)_2(Te,Se)_3$ and $(Pb,Sn)(Te,Se)$, because these compounds have the same required material features, including a narrow bandgap, heavy constituent elements, and large spin–orbit coupling.[30-37] Therefore, it is worth investigating the thermoelectric properties of $EuIn_2As(P)_2$ and $SrSn_2As_2$. Furthermore, unique and exotic transport properties have been reported in related materials. For example, a decrease in thermal conductivity was demonstrated for $NaSn_2As_2$ and $NaSnAs$, with emphasis on the existence of lone-pair electrons.[38] Moreover, low thermal conductivity has been demonstrated for $Li_{1-x}Sn_{2+x}As(P)_2$, mainly because of their local ordering.[39,40] Direction-dependent carrier polarity has been demonstrated for $NaSn_2As_2$ and $NaSnAs$, suggesting its applicability for transverse thermoelectric conversion.[41-43] In addition to being thermoelectric materials, these compounds are interesting because they undergo superconducting transitions at low temperatures.[44-48]

In this study, we determined the thermoelectric properties of the As/P-based Zintl compounds $EuIn_2As_{2-x}P_x$ ($x = 0$ to 2) and $SrSn_2As_2$. In the early stage of this work, we first investigated the thermoelectric properties of $SrSn_2As_2$. It was found that high carrier concentration ($\sim 10^{21}$ cm^{-3}) of undoped $SrSn_2As_2$—likely due to Sn vacancies—makes it difficult to optimize its thermoelectric properties. Then, we examined $EuIn_2As(P)_2$, aiming to decrease carrier concentration by replacing Sn by In. As expected, $EuIn_2As(P)_2$ exhibited carrier concentration of $\sim 10^{19}$ cm^{-3}. Furthermore, we prepared $EuIn_2As_{2-x}P_x$ solid solution to increase the thermoelectric properties. We have also used first-principles calculations to investigate the electronic structures and thermoelectric properties of these materials.
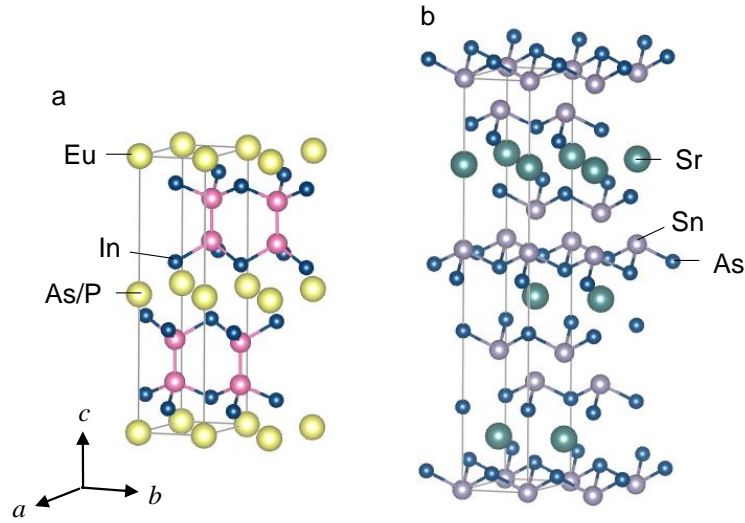
Figure 1. Schematic illustrations of the crystal structures of (a) EuIn2As$_{2-x}$P$_x$ and (b) SrSn$_2$As$_2$. The outlined regions represent the unit cells.

Methods

Sample preparation

We prepared polycrystalline $EuIn_2As_2$ by reacting EuAs, InAs, and In (99.99%) powder. We first prepared EuAs by reacting a Eu (99.9%) with As (99.9999%) in a 1:1 stoichiometric ratio at 800−850 °C for 20 h in a carbonized silica tube. We scraped the surface of the Eu ingot mechanically by filing it before use. We then cut or crushed the Eu ingot and As grains into small pieces to ensure feasibility of the reaction by increasing the surface area. We carried out carbonization of the silica tube via the evaporation of acetone. We prepared InAs by reacting In with As in a 1:1 stoichiometric ratio at 950 °C for 10 h in a sealed silica tube. Then, we prepared a stoichiometric mixture of EuAs, InAs, and In in a 1:1:1 ratio that we pelletized, placed in a carbon crucible, and heated at 900 °C for 40 h in a sealed silica tube.

Similarly, we synthesized $EuIn_2P_2$ by reacting EuP, InP, and In in a 1:1:1 stoichiometric ratio at 900 °C for 40 h. We prepared EuP by reacting Eu with P (99.999%) grains, which we crushed into powder, at 800−900 °C for 15 h in a carbonized silica tube. We then prepared InP by reacting In with P in a 1:1 stoichiometric ratio at 900 °C for 10 h in a sealed silica tube. We prepared $EuIn_2As_{2-x}P_x$ ($x = 0$, 0.1, 0.2, 0.6, 1, and 2) in the same manner. We prepared $SrSn_2As_2$ by reacting SrAs, SnAs, and Sn (99.99%) powder in a 1:1:1 stoichiometric ratio at 600 °C for 25 h. We prepared SrAs by reacting a Sr (99.9%) rod, which we cut into small pieces, with As in a 1:1 stoichiometric ratio at 800 °C for 20 h in a sealed silica tube. We prepared SnAs by reacting Sn with As in a 1:1 stoichiometric ratio at 500 °C for 18 h in a sealed silica tube.

We compressed the obtained samples by hot-pressing them in a graphite die at 50 MPa for 30 min. We pressed $EuIn_2As_{2-x}P_x$ at 800 °C and $SrSn_2As_2$ at 600 °C. We calculated the

geometric density of each sample to be >95% of the corresponding unit-cell density. It was found that the obtained samples endure at least 1 week of exposure to air without visible signs of oxidation/hydrolysis.

To examine the effects of different sample-preparation procedures, we prepared $EuIn_2As_2$ using ball-milling followed by hot-pressing. We placed stoichiometric amounts of Eu and InAs into a ZrO_2 vessel and milled them with ZrO_2 balls in a planetary ball-mill apparatus (Fritsch Pulverisette 7) at a rotation speed of 500 rpm for 6 h in an Ar atmosphere. After milling them, we placed the powders in graphite dies and hot-pressed them at 850 °C for 30 min.

Note that As is highly toxic and experiments related to this elements must be handled with extreme care. For instance, it is suggested to conduct extra-long purging after hot-pressing before the chamber is vented.

Sample characterization

We examined the chemical compositions of the obtained samples using energy-dispersive X-ray spectrometry (EDX; Oxford SwiftED3000). We measured the X-ray diffraction (XRD) patterns in the laboratory with CuKα radiation using a Rigaku Miniflex 600 equipped with a D/teX Ultra detector. In addition, we measured synchrotron X-ray diffraction (SXRD) patterns at BL02B2 of SPring-8 under proposal number 2020A1096. The diffraction data were collected using a high-resolution, one-dimensional, semiconductor detector MYTHEN.[49] The wavelength of the radiation beam was determined to be 0.495395(1) Å using a CeO_2 standard. We refined

the crystal-structure parameters by the Rietveld method using RIETAN-FP.[50] The crystal structure was visualized using VESTA.[51]

Transport measurements

We measured the Hall coefficient R_H using the five-probe method with a physical-property measurement system (Quantum Design). We calculated the Hall carrier concentration as $n = 1/R_H e$, where e is the charge of an electron. We measured the electrical resistivity and Seebeck coefficient using a four-probe method and a quasi-steady-state method, respectively (ZEM-3, Advanced Riko). We used pressure contact probes for these measurements. We measured the thermal diffusivity using a laser-flash method (TC1200-RH, Advanced Riko). We calculated the thermal conductivity using the relationship $\kappa = DC_p d$, where D, C_p, and d are the thermal diffusivity, specific heat, and sample density, respectively. We estimated C_p using the Dulong–Petit model, $C_p = 3n_a R$, where n_a is the number of atoms per formula unit, and R is the gas constant.

First-principles calculations

We performed first-principles band-structure calculations using VASP 5.4.4[52,53] to obtain the electronic structures of $EuIn_2As_2$, $EuIn_2P_2$, and $SrSn_2As_2$ by adopting the experimentally determined structure parameters for single crystals.[23-25] We calculated the electronic density, including spin–orbit coupling, self-consistently within the generalized gradient approximation proposed by Perdew, Burke, and Ernzerhof (PBE)[54] using a $9 \times 9 \times 2$ k-mesh for $EuIn_2As_2$ and

EuIn$_2$P$_2$ and an 18 × 18 × 18 k-mesh for SrSn$_2$As$_2$. The cutoff energy for the plane-wave basis set was fixed at 350 eV. For Eu, we used potentials obtained with the open-core treatment for the f-electrons. We calculated the Seebeck coefficient within Boltzmann transport theory, as implemented in the BoltzTrap2 code,[55] using a 44 × 44 × 9 k-mesh for EuIn$_2$As$_2$ and EuIn$_2$P$_2$ and a 25 × 25 × 25 k-mesh for SrSn$_2$As$_2$. We assumed the rigid-band approximation and constant relaxation time to calculate the Seebeck-coefficient tensors. For comparison with the experimental results for polycrystalline samples, we obtained the final results for the Seebeck coefficients by averaging over the xx, yy, and zz components of the Seebeck-coefficient tensor.

Results and Discussion

Crystal structures and chemical compositions

Figure 2 shows the SXRD pattern and the Rietveld refinement results for EuIn$_2$As$_{1.8}$P$_{0.2}$ ($x = 0.2$) as a representative sample. Most of the diffraction peaks can be assigned to space group $P6_3/mmc$, indicating that EuIn$_2$As$_{2-x}$P$_x$ is the primary phase. We estimated the amounts of impurity phases using Rietveld refinement: InAs (1.3 wt%) and In (1.2 wt%). We determined the lattice parameters of the end-member compounds ($x = 0$ and 2) to be $a = 4.21354(13)$ Å and $c = 17.9489(5)$ Å for $x = 0$ and $a = 4.06659(9)$ Å and $c = 17.5559(4)$ Å for $x = 2$, which are in agreement with previously reported results.[23,24] The lattice parameters of EuIn$_2$As$_{2-x}$P$_x$ change almost linearly with x, as shown in Figure 3. The chemical composition determined using EDX indicates that the sample composition is almost consistent with the nominal composition of the starting materials, as shown in Figure 4.

Similarly, most of the diffraction peaks from $SrSn_2As_2$ can be assigned to space group $R\bar{3}m$, as shown in Figure S2, and we determined the lattice parameters to be $a = 4.20467(3)$ Å and $c = 26.71906(19)$ Å, consistent with a previous report.[25] The chemical composition determined using EDX is Sr:Sn:As = 19.92(19):40.45(23):39.61(11) for $SrSn_2As_2$.
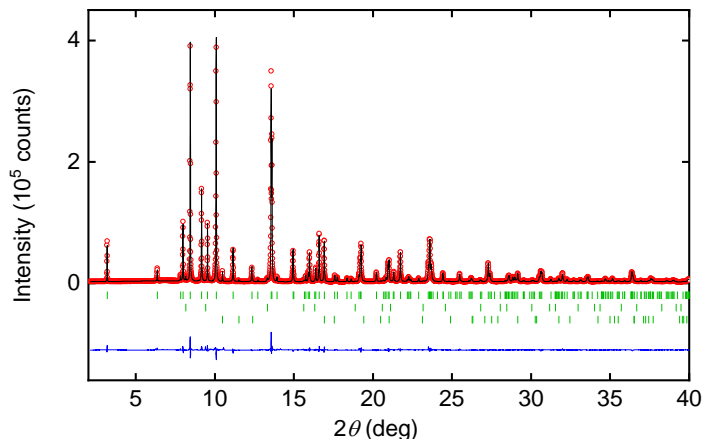
Figure 2. Observed SXRD pattern of $EuIn_2As_{1.8}P_{0.2}$ and the Rietveld refinement results. The circles (red) and solid lines (black) represent the observed and calculated patterns, respectively. The difference between the observed and calculated patterns is shown at the bottom (blue). The vertical marks (green) indicate the Bragg reflection positions for $EuIn_2As_{1.8}P_{0.2}$, InAs, and In, respectively, from upper to lower. Analogous data for other samples are shown in Figure S1 and S2 in the Supporting Information.
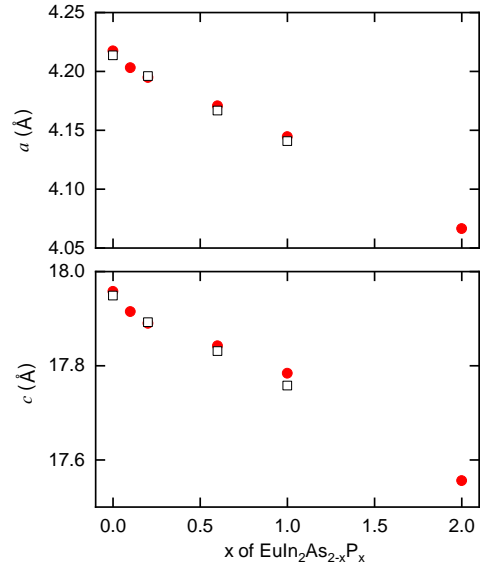
Figure 3. The lattice parameters a and c of $EuIn_2As_{2-x}P_x$ as functions of x. The results obtained using XRD with $CuK\alpha$ radiation (closed red circles) and using a synchrotron (open black squares) as the X-ray source are shown. The error bars are smaller than the symbols.
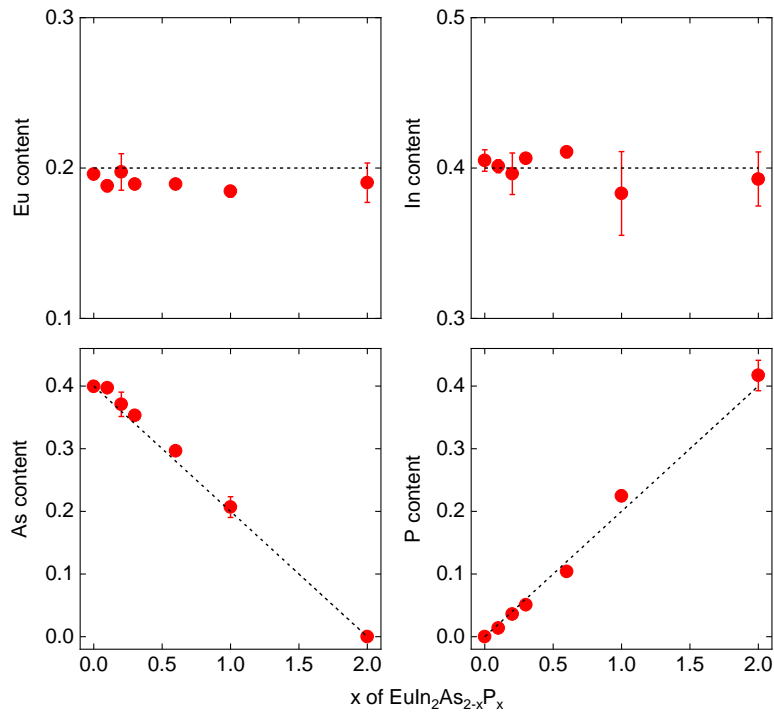
Figure 4. The chemical compositions of $EuIn_2As_{2-x}P_x$ as functions of x, obtained using EDX. The dashed lines represent the nominal compositions of the starting materials.

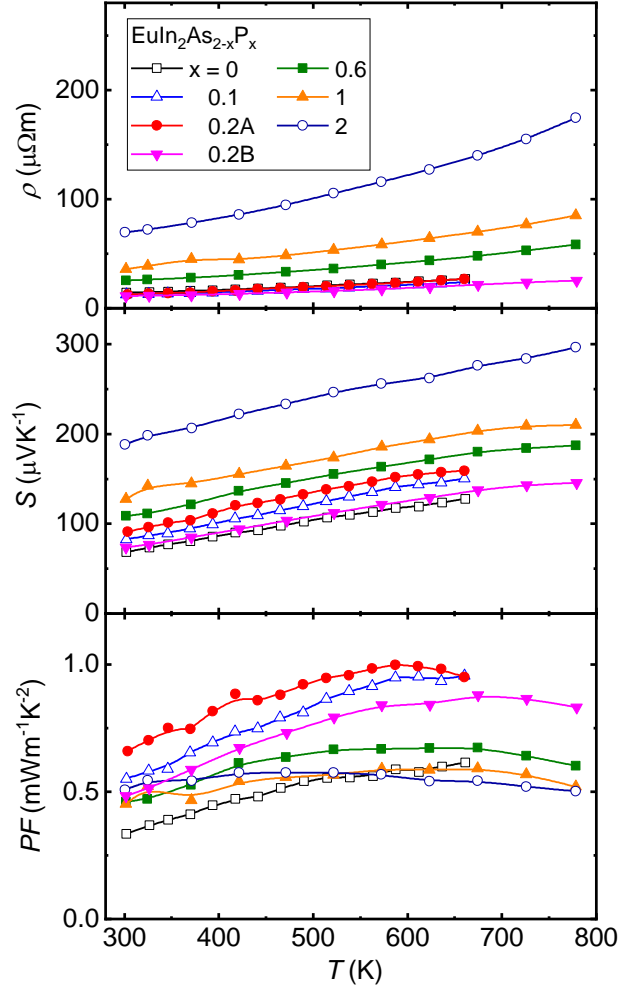**Electrical transport properties of $EuIn_2As_{2-x}P_x$**

Figure 5 shows the charge-carrier transport properties—the Hall carrier concentration, electrical resistivity, Hall carrier mobility, and Seebeck coefficient—as functions of x for $EuIn_2As_{2-x}P_x$ at 300 K. The positive signs of the Hall and Seebeck coefficients confirm that holes are the dominant carriers in these compounds. The Hall carrier concentration is on the order of 10^{19} cm^{-3}, and it tends to decrease with increasing x. For $x = 0$, the electrical resistivity and Seebeck coefficient are 14 $\mu\Omega$ m and 68 μV K^{-1}, respectively. Both the resistivity and the Seebeck coefficient tend to increase with increasing x, which is generally consistent with the change in carrier concentration. Assuming a single parabolic band and acoustic-phonon scattering,[56-58] the density-of-states effective mass is in the range 0.3–0.7 m_0, where m_0 is the rest mass of a free electron, as shown in Figure S3. The Hall carrier mobility is ~100 cm^2 V^{-1} s^{-1}, and the mobility decreased at $x = 0.6$ and 1. This is probably due to point-defect scattering of the carriers in the solid solution. Notably, these charge-carrier transport properties do not change linearly with x; this may correlate with electronic transitions between topologically nontrivial states and trivial states, as we discuss later with the aid of first-principles calculations. Notably, we obtained different values of the transport properties for different batches of samples with $x = 0.2$, although the XRD and EDX characterizations indicate that the purity and compositions of these samples are almost the same. We present both measurement results because we believe that these are also the valuable information. Hereafter, we denote these samples as $x = 0.2$A and 0.2B.

Figure 6 shows the temperature dependence of the transport properties of $EuIn_2As_{2-x}P_x$: the electrical resistivity, Seebeck coefficient, and electrical power factor ($S^2\rho^{-1}$). Both the electrical resistivity and the Seebeck coefficient increase with increasing temperature, as expected for a degenerate semiconductor. The calculated power factor reaches almost 1 mW m^{-1} K^{-2} at around 600 K for $x = 0.1$ and 0.2—which is almost twice that of the end-member compounds ($x = 0$ and 2)—because they have relatively low resistivities and high Seebeck coefficients. To examine the thermal stability, we have repeated measurements of electrical resistivity and Seebeck coefficient for $x = 0.2$. As shown in Figure S4, $x = 0.2$ exhibits very small thermal hysteresis in the repeated measurements up to 773 K, suggesting thermal stability of this sample to this temperature. We note that the direction-dependence of these transport measurements is not significant, as shown in Figure S5.
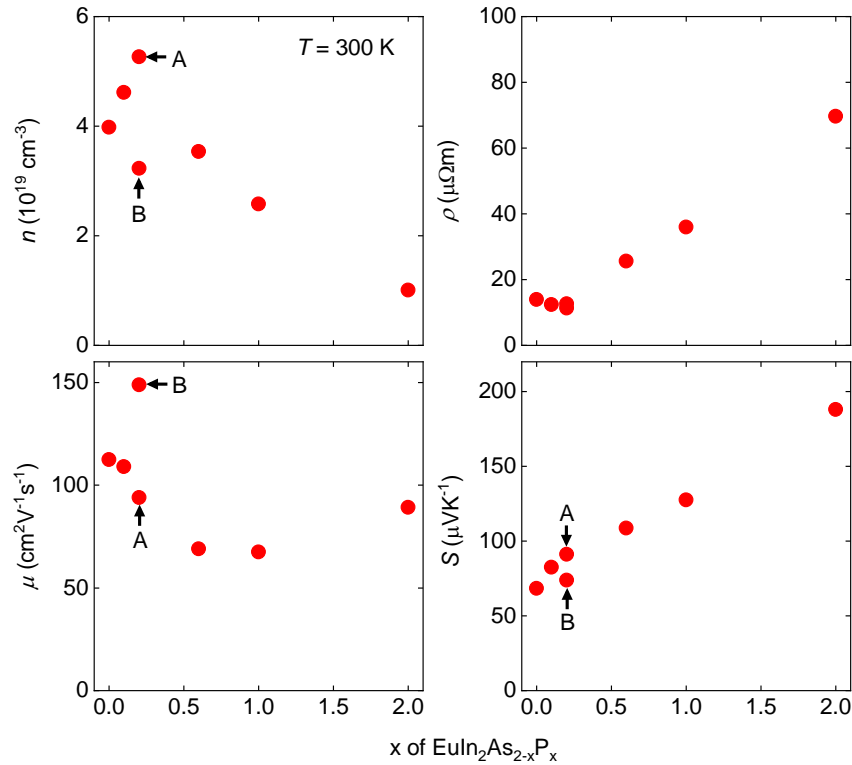
Figure 5. Charge-carrier transport properties at 300 K: the Hall carrier concentration n, electrical resistivity ρ, Hall carrier mobility μ, and Seebeck coefficient S for $EuIn_2As_{2-x}P_x$. For $x = 0.2$, measurement results for different batches of samples (labeled as A and B) are shown. The electrical resistivity of $x = 0.2A$ and $0.2B$ is almost coincident.

Figure 6. The electrical resistivity ρ, Seebeck coefficient S, and electrical power factor PF as a function of temperature T for $EuIn_2As_{2-x}P_x$.

Thermal transport properties and *ZT* for EuIn₂As₂₋ₓPₓ

Figure 7a shows thermal conductivity as a function of temperature for $EuIn_2As_{2-x}P_x$. We found the thermal conductivity at 300 K to be 3.9 W m⁻¹ K⁻¹ for $x = 0$ and 6.8 W m⁻¹ K⁻¹ for $x = 2$. The thermal conductivity is generally expressed as the sum of electronic and lattice components. The electronic thermal conductivity can be obtained from the Wiedemann–Franz relationship $\kappa_{el} = LT\rho^{-1}$, where L is the Lorentz number. We calculated L using the formula $L = 1.5 + \exp(S/116)$, where L and S are in units of 10^{-8} W Ω K⁻² and μV K⁻¹, repectively.[59] We obtained the lattice thermal conductivity by subtracting the electronic component from the total thermal conductivity. We evaluated the lattice thermal conductivities of the end-member compounds to be 3.4 W m⁻¹ K⁻¹ for $x = 0$ and 6.7 W m⁻¹ K⁻¹ for $x = 2$ at 300 K. The high value of κ_l at $x = 2$ ($EuIn_2P_2$) is in agreement with the general view that a lighter constituent leads to a higher value of κ_l because of its high phonon group velocity.[60] The lattice thermal conductivity decreases with increasing temperature, indicating that the Umklapp process is the dominant phonon-scattering process in these compounds. The lattice thermal conductivity as a function of x is shown in Figure 7b. For $x \leq 1$, the lattice thermal conductivity is almost unchanged. This is probably due to at least two contributions: (i) an increase in κ_l owing to the increase in the phonon group velocity with increasing x and (ii) a decrease in κ_l because of increased point-defect scattering in the solid solution; i.e., the so-called *alloy scattering*.[61,62]

Figure 8 shows the calculated *ZT* for $EuIn_2As_{2-x}P_x$. The value of *ZT* reaches 0.29 at 773 K for $x = 0.2B$, which is almost twice that of the end-member compounds. This is mainly because of the increased power factor while lattice thermal conductivity is reduced by alloy scattering, as described above.

Furthermore, we investigated the different sample-preparation procedures for $EuIn_2As_2$. Ball-milling followed by hot-pressing has been employed to synthesize various thermoelectric Zintl compounds.[8-15] In addition, enhanced thermoelectric properties were demonstrated for classic thermoelectric materials, such as $Si_{1-x}Ge_x$[63] and $(Bi,Sb)_2Te_3$,[64] by using ball-milling owing to the reduced particle size. Figures S6 and S7 show the thermoelectric transport properties of $EuIn_2As_2$ prepared using both the solid-state reaction technique and ball-milling followed by hot-pressing. These samples exhibit almost identical transport properties, confirming that the electrical and thermal transport properties described above are indeed intrinsic properties of the polycrystalline $EuIn_2As_2$. These results also support the reproducibility of the present work.

In preliminary experiments, we have also investigated the thermoelectric properties of $Eu_{1-x}Sr_xIn_2As_2$ ($x \leq 0.3$). We expected a decrease in the lattice thermal conductivity because of increased point-defect scattering caused by Sr doping. Characterization results of $Eu_{1-x}Sr_xIn_2As_2$ using XRD and EDX are shown in Figure S8–S10. Regrettably, the electrical and thermal transport properties were barely changed because of Sr doping, as shown in Figure S11.
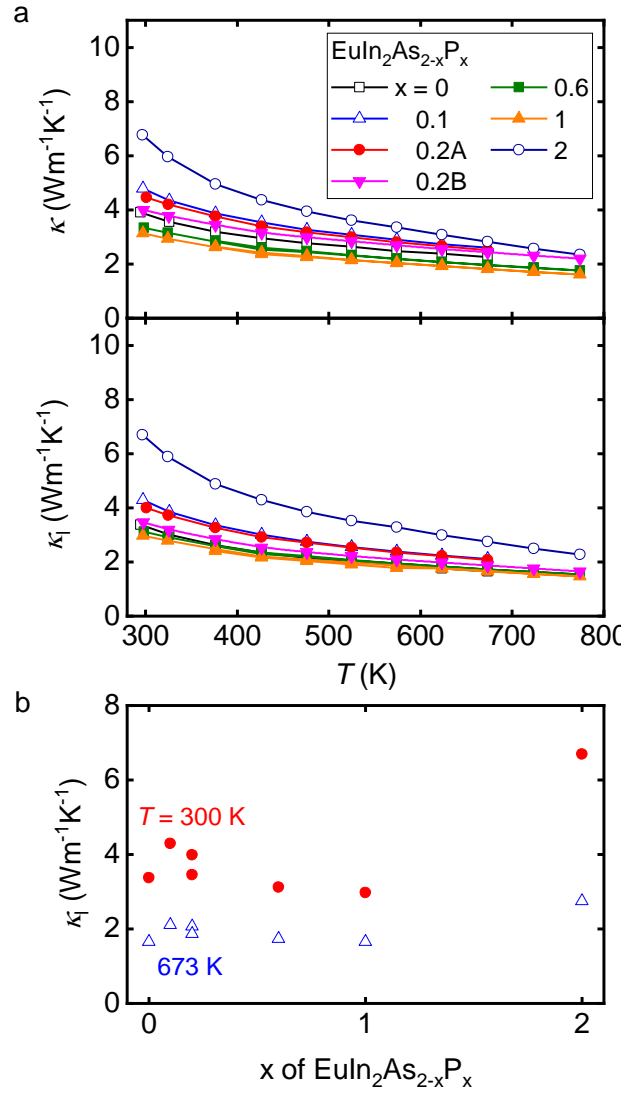
Figure 7. (a) Temperature dependence of the total thermal conductivity κ and of the lattice thermal conductivity κ_l of $EuIn_2As_{2-x}P_x$. (b) κ_l versus x for $EuIn_2As_{2-x}P_x$ at 300 K and at 673 K.
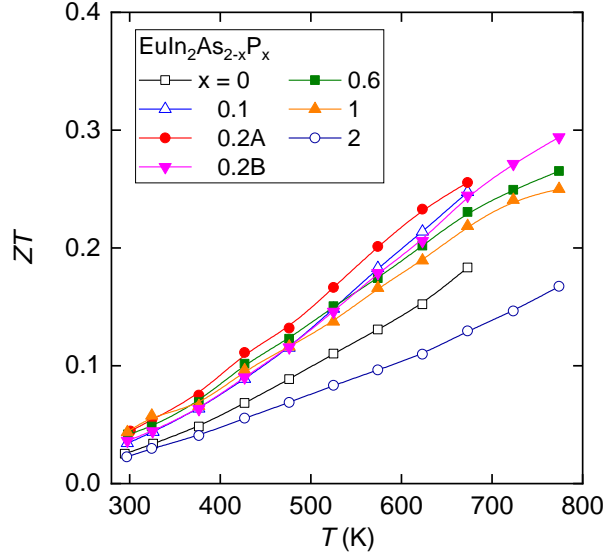
Figure 8. The dimensionless figure of merit ZT as a function of temperature T for $EuIn_2As_{2-x}P_x$.

Thermoelectric properties of $SrSn_2As_2$

The typical transport properties of $SrSn_2As_2$ at 300 K are as follows: a Hall carrier concentration of 1.6×10^{21} cm^{-3}, an electrical resistivity of 3.7 $\mu\Omega$ m, a Hall carrier mobility of 11 cm^2 V^{-1} s^{-1}, and a Seebeck coefficient of 37 μV K^{-1}. Undoped $SrSn_2As_2$ has a high hole concentration, probably because of self-doping by the hole-donating Sn vacancies, which occurs similarly in other Sn-containing compounds, such as SnTe.[65] To suppress the Sn vacancies, we prepared several batches of $SrSn_2As_2$ under different conditions, including Sn-rich compositions of the raw materials. However, our preliminary experiments show that tuning the carrier concentration seems to be difficult for $SrSn_2As_2$. It should be noted that some of Zintl-phase compounds show high hole concentration due to vacancies of cations (such as Eu, Sr, and Yb).[66,67] Indeed, we have no experimental evidence of Sn vacancies, which is not easy to detect

in experiments. However, it was reported that $EuSn_2As_2$ shows low electrical resistivity and Seebeck coefficient (for example, $\rho < 10$ $\mu\Omega$m at 300 K and $S = 28$ μV/K at 373 K).[68,69] This result suggests that high hole concentration of $SrSn_2As_2$ is resulted from Sn vacancy, rather than Sr vacancy.

Figure 9 shows the charge-carrier transport properties of $SrSn_2As_2$ as a function of temperature. We observed slight differences in different batches of samples, suggesting that the electrical transport properties are affected by the sample stoichiometry. In addition, we observed a dependence on the direction in which the measurements were performed. Figure 10 shows the thermal conductivity of $SrSn_2As_2$ versus temperature. It is noteworthy that the lattice thermal conductivity is approximately comparable to that of $EuIn_2As_2$, and it is higher than that of $NaSn_2As_2$. Previous studies have demonstrated that the value of κ_l for NaSnAs is lower than that of $NaSn_2As_2$ because of the effects of double lone-pair electrons;[38] i.e., $NaSn_2As_2$ has lone-pairs only in the As atoms, while NaSnAs has lone-pairs in both the As and Sn atoms. According to a simple ionic-bonding model, $SrSn_2As_2$ may also have double lone-pairs in As and Sn, where schematic illustrations of the crystal structures of NaSnAs, $Na(Sr)Sn_2As_2$, and $EuIn2As(P)_2$ are shown in Fig. S12. However, this scenario does not seem to be supported by the high lattice thermal conductivity of $SrSn_2As_2$ because $SrSn_2As_2$ is better categorized as a Zintl compound, $Sr^{2+}[SnAs]^{2-}$, rather than by a simple ionic description such as $Sr^{2+}Sn^{2+}{}_2As^{3-}{}_2$. However, X-ray photoemission spectroscopy of $SrSn_2As_2$ shows that the Sn $4d$ and $5d$ spectra are similar to those of SnO, implying that Sn is in the ionic state Sn^{2+} in $SrSn_2As_2$.[70] Further studies will be required to elucidate the actual nature of the chemical bonding in $SrSn_2As_2$.
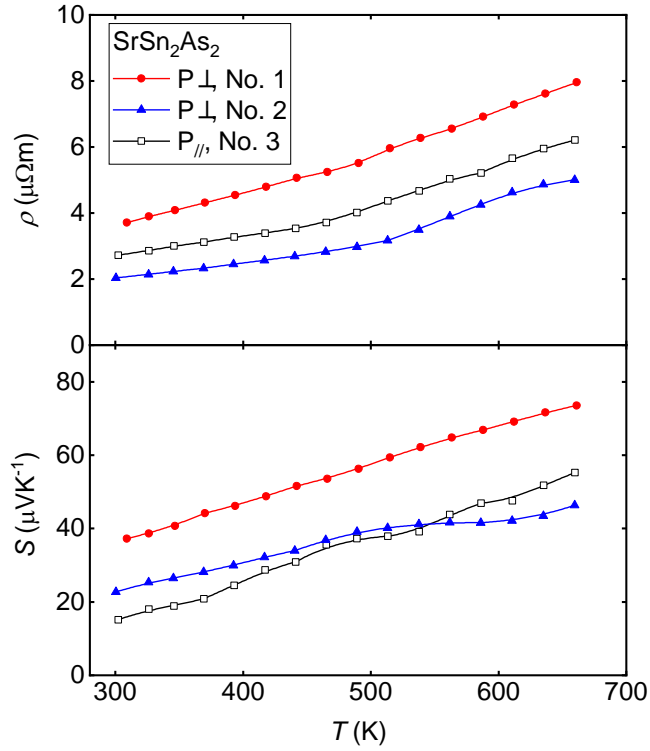
Figure 9. The electrical resistivity ρ and the Seebeck coefficient S as functions of temperature T for SrSn$_2$As$_2$.
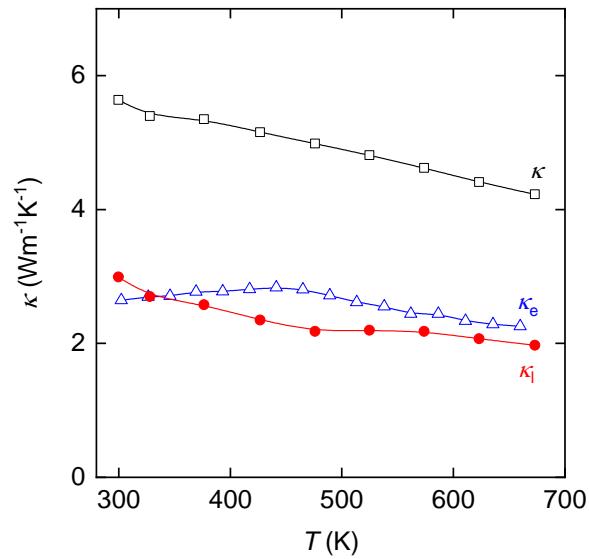
Figure 10. The temperature dependence of the total thermal conductivity κ, the electrical thermal conductivity κ_e, and the lattice thermal conductivity κ_l of SrSn$_2$As$_2$.

First-principles calculations

Figure 11 shows the electronic band structures of $EuIn_2As_2$, $EuIn_2P_2$, and $SrSn_2As_2$. For $EuIn_2As(P)_2$, the valence band around the Fermi level originates mainly from the As(P) p_z orbital. The top of the p_z band of $EuIn_2As_2$ is positioned ~0.1 eV above the Fermi energy; therefore, the bandgap originates from mixing between the conduction and valence bands due to spin–orbit coupling. It is shown that $EuIn_2As_2$ can exhibit a nontrivial topological electronic state, as discussed in the reports by Xu et al.[26] and Sato et al.[27] When As is substituted by P, the top of the p_z band sinks below the Fermi level. $EuIn_2P_2$ is therefore a semiconductor with a bandgap of ~0.4 eV. $SrSn_2As_2$ is also a topologically nontrivial material with band inversion, as reported by Gibson et al.[28] and Rong et al.[29]

Figure 12 shows the densities of states (DOSs) of $EuIn_2As_2$, $EuIn_2P_2$, and $SrSn_2As_2$. The density of states in $SrSn_2As_2$ near the Fermi energy is larger than that in $EuIn_2As(P)_2$. This can be understood from the band structure along the Γ–A and Γ–Z lines (Fig. 11), where the A and Z points are $(0, 0, \pi/c)$ and $(0, 0, 3\pi/c)$, respectively. Although the length of the Γ–Z line for $SrSn_2As_2$ is longer than the lengths of the Γ–A lines for $EuIn_2As(P)_2$, the valence-band energy difference between the Γ and Z (A) points is ~1 eV for $EuIn_2As(P)_2$ and 0.5 eV for $SrSn_2As_2$, which results in the difference in the DOS effective mass between them. Notably, the DOS near the Fermi energy of $SrSn_2As_2$ has the character of As p-orbitals and Sn s/p-orbitals while that of $EuIn_2As(P)_2$ mainly consists of the As(P) p_z orbital.

Figure 13 shows the calculated results for the Seebeck coefficient plotted against carrier concentration at 300 K; they are roughly in agreement with the experimental results. First-principles calculations tend to underestimate the Seebeck coefficient[71–73]. In particular, there is a

large difference between the calculated and experimental Seebeck coefficient for $EuIn_2P_2$. This may be because the Boltzmann transport theory cannot be applied at this low carrier concentration, where the chemical potential is positioned within the bandgap. Because of the small bandgaps of $EuIn_2As_2$ and $SrSn_2As_2$, the Seebeck coefficient is maximum in the low-carrier-concentration regime. Comparing the carrier concentration dependence of the Seebeck coefficient of all the compounds, we observed that $SrSn_2As_2$ has a large Seebeck coefficient at $\sim 10^{20}$ cm^{-3} owing to the difference in the effective mass, as described above. The temperature dependence of the Seebeck coefficient shown in Figure S13 indicates that the bandgap of $EuIn_2P_2$ is expected to be larger than the theoretically obtained value (0.4 eV) because the calculated Seebeck coefficient of $EuIn_2P_2$ is maximized at ~ 800 K, whereas the experimental result increases linearly with increasing temperature. The calculated power factor is maximized at $\sim 1 \times 10^{19}$ cm^{-3} so that the experimental carrier concentration of $EuIn_2P_2$ is near the optimal doping level.

Notably, both $EuSn_2As_2$ and $EuSn_2P_2$ have been shown to be intrinsic magnetic topological insulators through first-principles calculations and angle-resolved photoemission spectroscopy.[66,74,75] This contrasts with the results of our calculations, which indicate that a nontrivial topological electronic structure for $EuIn_2As_2$ turns into a trivial electronic structure for $EuIn_2P_2$. Consequently, the solid solution of $EuIn_2As_{2-x}P_x$ may provide an attractive stage for exploring quantum phase transitions between topologically nontrivial electronic states and conventional semiconducting states, which is also fascinating for efficient thermoelectric materials.[36,37]
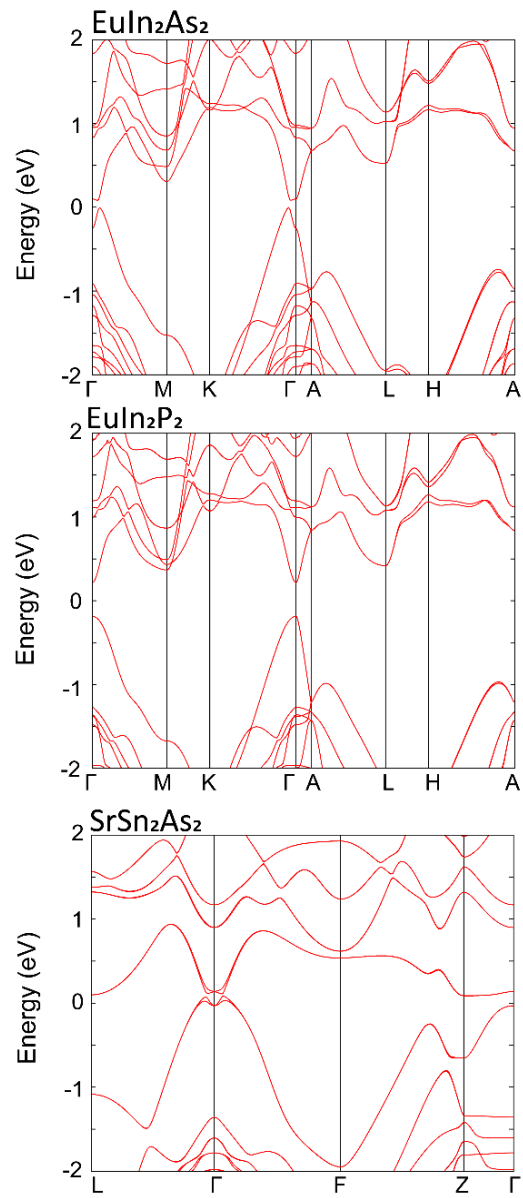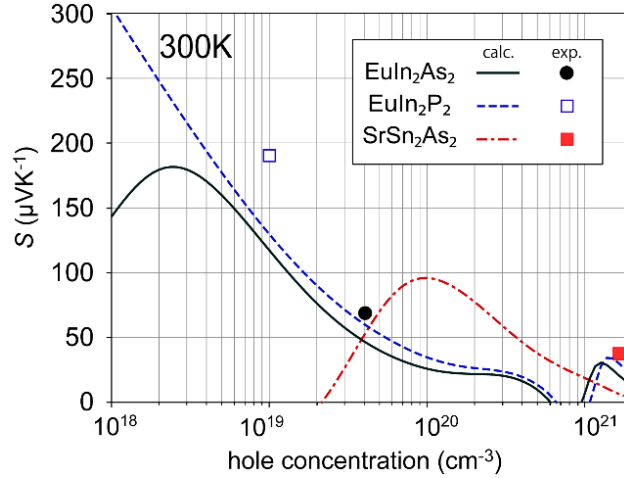
Figure 11. Band structures of $EuIn_2As_2$, $EuIn_2P_2$, and $SrSn_2As_2$.
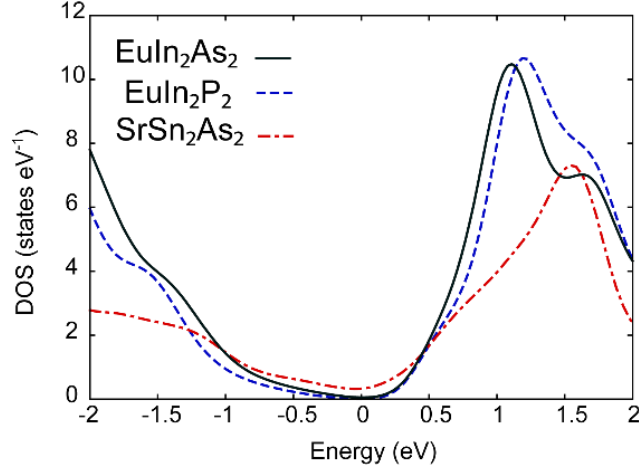
Figure 12. The densities of states (DOSs) in $EuIn_2As_2$, $EuIn_2P_2$, and $SrSn_2As_2$.

Figure 13. Hole concentration dependence of the calculated and measured Seebeck coefficients of $EuIn_2As_2$, $EuIn_2P_2$, and $SrSn_2As_2$ at 300 K.

Conclusion

In summary, we have investigated the thermoelectric properties of the A/P-based Zintl compounds $EuIn_2As_{2-x}P_x$ and $SrSn_2As_2$. With a carrier concentration of $\sim 10^{19}$ cm^{-3}, $EuIn_2As_{2-x}P_x$

shows promising transport properties, including an electrical power factor of ~1 mW m^{-1} K^{-2} and a dimensionless ZT of 0.29 at 773 K. On the other hand, a reduced carrier concentration is required to optimize the thermoelectric properties of SrSn$_2$As$_2$, which has been challenging to obtain in our experiments so far. Furthermore, there seems to be room for decreasing the lattice thermal conductivity to improve ZT. First-principles calculations strongly suggest the possible existence of a phase transition between topologically nontrivial electronic states and conventional semiconducting states in EuIn$_2$As$_{2-x}$P$_x$, making this system an attractive stage for exploring topological states as well as efficient thermoelectric materials.

ASSOCIATED CONTENT

Supporting Information

The Supporting Information is available free of charge on the ACS Publications website.
SXRD patterns of EuIn$_2$As$_{2-x}$P$_x$, Seebeck coefficient as a function of carrier concentration for EuIn$_2$As$_{2-x}$P$_x$, repeated measurements of carrier transport of $x = 0.2$, XRD and thermoelectric properties of EuIn$_2$As$_2$ prepared using ball-milling, sample characterization and thermoelectric properties of Eu$_{1-x}$Sr$_x$In$_2$As$_2$ ($x \leq 0.3$), schematic illustration of the crystal structure of NaSnAs, temperature dependence of the experimentally and theoretically determined Seebeck coefficients (PDF)

AUTHOR INFORMATION

Corresponding Author

*E-mail for Y. G.: y_goto@tmu.ac.jp, E-mail for H. U.: hidetomo.usui@riko.shimane-u.ac.jp

Author Contributions

K. S. and Y. G. carried out sample preparation, crystal structure analysis, and thermoelectric measurements. Y. G., K. H. R. K., N. N. measured Hall coefficient. K. S., A. M., C. M., Y. K. conducted SXRD measurements. H. U. performed first-principles calculations. Y. G. and H. U. wrote the manuscript. All authors discussed the results and commented on the work.

Notes

The authors declare no competing financial interest.

REFERENCES

(1) Snyder, G. J.; Toberer, E. S. Complex thermoelectric materials. *Nat. Mater.* **2008**, *7*, 105–114.

(2) Zeier, W. G.; Zevalkink, A.; Gibbs, Z. M.; Hautier, G.; Kanatzidis, M. G.; Snyder, G. J. Thinking like a chemist: intuition in thermoelectric materials. *Angew. Chem. Int. Ed.* **2016**, *55*, 6826–6841.

(3) Zhao, L. D.; Dravid, V. P.; Kanatzidis, M. G. The panoscopic approach to high performance thermoelectrics. *Energy Environ. Sci.* **2014**, *7*, 251–268.

(4) Sootsman, J. R.; Chung, D. Y.; Kanatzidis, M. G. New and old concepts in thermoelectric materials. *Angew. Chem. Int. Ed.* **2009**, *48*, 8616–8639.

(5) Kauzlarich, S. M.; Brown, S. R.; Snyder, G. J. Zintl Phases for Thermoelectric Devices. *Dalton Trans*. **2007**, *21*, 2099−2107.

(6) Toberer, E. S.; May, A. F.; Snyder, G. J. Zintl Chemistry for Designing High Efficiency Thermoelectric Materials. *Chem. Mater.* **2010**, *22*, 624–634.

(7) Shuai, J.; Mao, J.; Song, S.; Zhang, Q.; Chen, G.; Ren, Z. Recent progress and future challenges on thermoelectric Zintl materials. *Mater. Today Phys.* **2017**, *1*, 74–95.

(8) Wang, X.-J.; Tang, M.-B.; Chen, H.-H.; Yang, X.-X.; Zhao, J.-T.; Burkhardt, U.; Grin, Y. Synthesis and high thermoelectric efficiency of Zintl phase $YbCd_{2−x}Zn_xSb_2$. *Appl. Phys. Lett*. **2009**, *94*, 092106.

(9) Grebenkemper, J. H.; Hu, Y.; Barrett, D.; Gogna, P.; Huang, C. K.; Bux, S. K.; Kauzlarich, S. M. High Temperature Thermoelectric Properties of $Yb_{14}MnSb_{11}$ Prepared from Reaction of MnSb with the Elements. *Chem. Mater.* **2015**, *27*, 5791–5798.

(10) Zevalkink, A., Zeier, W.G., Pomrehn, G., Schechtel, E., Tremel, W., and Snyder, G.J. Thermoelectric properties of Sr_3GaSb_3—a chain-forming Zintl compound. *Energ. Environ. Sci.* **2012**, *5*, 9121.

(11) Zevalkink, A.; Swallow, J.; Ohno, S.; Aydemir, U.; Bux, S.; Snyder, G. J. Thermoelectric properties of the $Ca_5Al_{2-x}In_xSb_6$ solid solution. *Dalton Trans.* **2014**, *43*, 15872–15878.

(12) Ohno, S.; Aydemir, U.; Amsler, M.; Pöhls, J. H.; Chanakian, S.; Zevalkink, A.; White, M. A.; Bux, S. K.; Wolverton, C.; Snyder, G. J. Achieving zT > 1 in Inexpensive Zintl Phase $Ca_9Zn_{4+x}Sb_9$ by Phase Boundary Mapping. *Adv. Funct. Mater.* **2017**, *27*, 1606361–1606370.

(13) Tamaki, H.; Sato, H. K.; Kanno, T. Isotropic Conduction Network and Defect Chemistry in $Mg_{3+\delta}Sb_2$-Based Layered Zintl Compounds with High Thermoelectric Performance. *Adv. Mater.* **2016**, *28*, 10182−10187.

(14) Zhang, J.; Song, L.; Pedersen, S. H.; Yin, H.; Hung, L. T.; Iversen, B. B. Discovery of high-performance low-cost n-type Mg_3Sb_2-based thermoelectric materials with multi-valley conduction bands. *Nat. Comm.* **2017**, *8*, 13901.

(15) Chen, C.; Xue, W.; Li, S.; Zhang, Z.; Li, X.; Wang, X.; Liu, Y.; Sui, J.; Liua, X.; Caod, F.; Renf, Z.; Chuf, C.-W.; Wangc, Y.; Zhang, Q. Zintl-phase Eu_2ZnSb_2 : A promising thermoelectric material with ultralow thermal conductivity *Proc. Natl. Acad. Sci. U. S. A.* **2019**, *116*, 2831–2836.

(16)   Ponnambalam, V.; Lindsey, S.; Xie, W.; Thompson, D.; Drymiotis, F.; Tritt, T. M. High

Seebeck coefficient $AMXP_2$ (A = Ca and Yb; M, X = Zn, Cu and Mn) Zintl phosphides as

high-temperature thermoelectric materials. *J. Phys. D: Appl. Phys.* **2011**, *44*, 155406.

(17)   Ponnambalam, V.; Morelli, D. T. Thermoelectric Properties of Light-Element-Containing

Zintl Compounds $CaZn_{2-x}Cu_xP_2$ and $CaMnZn_{1-x}Cu_xP_2$ (x = 0.0−0.2). J. Electron. Mater.

2014, *43*, 1875−1880.

(18)   Kihou, K.; Nishiate, H.; Yamamoto, A.; Lee, C. H. Thermoelectric Properties of As-

Based Zintl Compounds $Ba_{1-x}K_xZn_2As_2$. *Inorg. Chem.* **2017**, *56*, 3709−3712.

(19)   Kunioka, H.; Kihou, K.; Nishiate, H.; Yamamoto, A.; Usui, H.; Kuroki, K.; Lee, C. H.

Thermoelectric properties of $(Ba,K)Cd_2As_2$ crystallized in the $CaAl_2Si_2$-type structure.

Dalton Trans. **2018**, *47*, 16205−16210.

(20)   Kunioka, H.; Kihou, K.; Kato, D.; Usui, H.; Iida, T.; Nishiate, H.; Kuroki, K.;

Yamamoto, A.; Lee, C. H. Thermoelectric Properties of $(Ba,K)Zn_2As_2$ Crystallized in the

$ThCr_2Si_2$-type Structure. *Inorg. Chem.* **2020**, *59*, 5828–5834.

(21)   Rajput, K.; Baranets, S.; Bobev, S. Observation of an unexpected n-type semiconducting

behavior in the new ternary Zintl phase Eu_3InAs_3. *Chem. Mater.* **2020**, *32*, 9616–9626.

(22)   Kamihara, Y.; Watanabe, T.; Hirano, M.; Hosono, H. Iron-based layered superconductor

$La[O_{1-x}F_x]FeAs$ (x = 0.05-0.12) with T_c = 26 K. *J. Am. Chem. Soc.* **2008**, *130*, 3296–3297.

(23)   Jiang, J.; Kauzlarich, S. M. Colossal magnetoresistance in a rare earth Zintl compound

with a new structure type: $EuIn_2P_2$. *Chem. Mater.* **2006**, *18*, 435–441.

(24)   Goforth, A. M.; Klavins, P.; Fettinger, J. C.; Kauzlarich, S. M. Magnetic properties and negative colossal magnetoresistance of the rare earth Zintl phase $EuIn_2As_2$. *Inorg. Chem.* **2008**, *47*, 11048–11056.

(25)   Eisenmann, B.; Klein, J. Zintl-Phasen mit Schichtanionen: Darstellung und Kristallstrukturen der isotypen Verbindungen $SrSn_2As_2$ und sowie eine Einkristallstrukturbestimmung von KSnSb. *Z. Anorg. Allg. Chem.* **1991**, *598/599*, 93–102.

(26)   Xu, Y.; Song, Z.; Wang, Z.; Weng, H.; Dai, X. Higher-Order Topology of the Axion Insulator $EuIn_2As_2$. *Phys. Rev. Lett.* **2019**, *122*, 256402.

(27)   Sato, T.; Wang, Z.; Takane, D.; Souma, S.; Cui, C.; Li, Y.; Nakayama, K.; Kawakami, T.; Kubota, Y.; Cacho, C.; Kim, T. K.; Arab, A.; Strocov, V. N.; Yao, Y.; Takahashi, T. Signature of band inversion in the antiferromagnetic phase of axion insulator candidate $EuIn_2As_2$. *Phys. Rev. Res.* **2020**, *2*, 33342.

(28)   Gibson, Q. D.; Schoop, L. M.; Muechler, L.; Xie, L. S.; Hirschberger, M.; Ong, N. P.; Car, R.; Cava, R. J. Three-dimensional Dirac semimetals: Design principles and predictions of new materials. *Phys. Rev. B* **2015**, *91*, 205128–205138.

(29)   Rong, L. Y.; Ma, J. Z.; Nie, S. M.; Lin, Z. P.; Li, Z. L.; Fu, B. . B.; Kong, L. Y.; Zhang, Z. Z.; Huang, Y. B.; Weng, H. M.; Qian, T.; Ding, H.; Tai, R. Z. Electronic structure of $SrSn_2As_2$ near the topological critical point. *Sci. Rep.* **2017**, *7*, 6133–6138.

(30)   Fu, C.; Sun, Y.; Felser, C. Topological thermoelectrics. *APL Mater.* **2020**, *8*, 040913.

(31)   Müchler, L.; Casper, F.; Yan, B.; Chadov, S.; Felser, C. Topological insulators and thermoelectric materials. *Phys. Status Solidi - Rapid Res. Lett.* **2013**, *7*, 91–100.

(32)   Ivanov, Y. V.; Burkov, A. T.; Pshenay-Severin, D. A. Thermoelectric Properties of Topological Insulators. *Phys. Status Solidi Basic Res.* **2018**, *255*, 1800020.

(33)   Xu, N.; Xu, Y.; Zhu, J. Topological insulators for thermoelectrics. *npj Quantum Mater.* **2017**, *2*, 51.

(34)   Müchler, L.; Zhang, H.; Chadov, S.; Yan, B.; Casper, F.; Kübler, J.; Zhang, S. C.; Felser, C. Topological insulators from a chemist's perspective. *Angew. Chemie - Int. Ed.* **2012**, *51*, 7221–7225.

(35)   Gooth, J.; Schierning, G.; Felser, C.; Nielsch, K. Quantum materials for thermoelectricity. *MRS Bulletin,* **2018**, *43*, 187-192.

(36)   Roychowdhury, S.; Samanta, M.; Banik, A.; Biswas, K. Thermoelectric energy conversion and topological materials based on heavy metal chalcogenides. *J. Solid State Chem.* **2019**, *275*, 103–123.

(37)   Lin, C.-C.; Kim, G.; Ginting, D.; Ahn, K.; Rhyee, J.-S. Enhancement of Thermoelectric Performances in a Topological Crystal Insulator $Pb_{0.7}Sn_{0.3}Se$ via Weak Perturbation of the Topological State and Chemical Potential Tuning by Chlorine Doping. *ACS Appl. Mater. Interfaces*, **2018**, *10*, 10927–10934.

(38)   Lin, Z.; Wang, G.; Le, C.; Zhao, H.; Liu, N.; Hu, J.; Guo, L.; Chen, X. Thermal

conductivities in NaSnAs, NaSnP, and $NaSn_2As_2$: effect of double lone-pair electrons. *Phys.*

Rev. B **2017**, *95*, 165201–165207.

(39)   Lee, K.; Kaseman, D.; Sen, S.; Hung, I.; Gan, Z.; Gerke, B.; Po, R.; Feygenson, M.;

Neuefeind, J.; Lebedev, O. I.; Kovnir, K. Intricate Short-Range Ordering and Strongly

Anisotropic Transport Properties of $Li_{1−x}Sn_{2+x}As_2$. *J. Am. Chem. Soc.* **2015**, *137*, 3622–3630.

(40)   Goto, Y.; Nakanishi, S.; Nakai, Y.; Mito, T.; Miura, A.; Moriyoshi, C.; Kuroiwa, Y.;

Usui, H.; Matsuda, T. D.; Aoki, Y.; Nakacho, Y.; Yamada, Y.; Kanamura, K.; Mizuguchi,

Y. The crystal structure and electrical/thermal transport properties of $Li_{1−x}Sn_{2+x}P_2$ and its

performance as a Li-ion battery anode material. *J. Mater. Chem. A* **2021**, *9*, 7034–7041.

(41)   He, B.; Wang, Y.; Arguilla, M. Q.; Cultrara, N. D.; Scudder, M. R.; Goldberger, J. E.;

Windl, W.; Heremans, J. P. The Fermi surface geometrical origin of axis-dependent

conduction polarity in layered materials. *Nat. Mater.* **2019**, *18*, 568–572.

(42)   Ochs, A. M.; Gorai, P.; Wang, Y.; Scudder, M. R.; Koster, K.; Moore, C. E.; Stevanovic,

V.; Heremans, J. P.; Windl, W.; Toberer, E. S.; Goldberger, J. E. Computationally Guided

Discovery of Axis-Dependent Conduction Polarity in NaSnAs Crystals. *Chem. Mater.* **2021**,

33, 946–951.

(43)   Nakamura, N.; Goto, Y.; Mizuguchi, Y. Axis-dependent carrier polarity in polycrystalline

$NaSn_2As_2$. *Appl. Phys. Lett.* (in press)

(44)   Goto, Y.; Yamada, A.; Matsuda, T. D.; Aoki, Y.; Mizuguchi, Y. SnAs-Based Layered

Superconductor $NaSn_2As_2$. *J. Phys. Soc. Jpn.* **2017**, *86*, 123701–123704.

(45)   Cheng, E. J.; Ni, J. M.; Meng, F. Q.; Ying, T. P.; Pan, B. L.; Huang, Y. Y.; Peets, D.; Zhang, Q. H.; Li, S. Y. Nodeless superconductivity in the SnAs-based van der Waals type superconductor $NaSn_2As_2$. *EPL* **2018**, *123*, 47004–47009.

(46)   Ishihara, K.; Takenaka, T.; Miao, Y.; Tanaka, O.; Mizukami, Y.; Usui, H.; Kuroki, K.; Konczykowski, M.; Goto, Y.; Mizuguchi, Y.; Shibauchi, T. Evidence for *s*-wave pairing with atomic scale disorder in the van der Waals superconductor $NaSn_2As_2$. *Phys. Rev. B* **2018**, *98*, 020503–020507.

(47)   Goto, Y.; Miura, A.; Moriyoshi, C.; Kuroiwa, Y.; Matsuda, T. D.; Aoki, Y.; Mizuguchi, Y. $Na_{1-x}Sn_2P_2$ as a new member of van der Waals-type layered tin pnictide superconductors. *Sci. Rep.* **2018**, *8*, 12852–12859.

(48)   Yuwen, H.; Goto, Y.; Jha, R.; Miura, A.; Moriyoshi, C.; Kuroiwa, Y.; Matsuda, D.; Aoki, Y.; Mizuguchi, Y. Enhanced superconductivity by Na doping in SnAs-based layered compound. *Jpn. J. Appl. Phys.* **2019**, *58*, 083001–083006.

(49)   Kawaguchi, S.; Takemoto, M.; Osaka, K.; Nishibori, E.; Moriyoshi, C.; Kubota, Y.; Kuroiwa, Y.; Sugimoto, K. High-throughput powder diffraction measurement system consisting of multiple MYTHEN detectors at beamline BL02B2 of SPring-8. *Rev. Sci. Instrum.* **2017**, *88*, 085111–085119.

(50)   Izumi, F.; Momma, K. Three-dimensional Visualization in Powder Diffraction. *Solid State Phenom.* **2007**, *130*, 15.

(51)   Momma, K.; Izumi, F. VESTA 3 for three-dimensional visualization of crystal, volumetric and morphology data. *J. Appl. Crystallogr*. **2011**, *44*, 1272-1276.

(52)   Kresse, G.; Furthmüller, J. Efficient iterative schemes for ab initio total-energy

         calculations using a plane-wave basis set. *Phys. Rev. B* **1996**, 54, 11169–11186.

(53)   Kresse, G.; Joubert, D. From ultrasoft pseudopotentials to the projector augmented-wave

         method. *Phys. Rev. B* **1999**, 59, 1758–1775.

(54)   Perdew, J. P.; Burke, K.; Ernzerhof, M. Generalized Gradient Approximation Made

         Simple. *Phys. Rev. Lett.* **1996**, 77, 3865–3868.

(55)   Madsen, G. K. H.; Carrete, J.; Verstraete, M. J.; BoltzTraP2, a program for interpolating

         band structures and calculating semi-classical transport coefficients. *Comput. Phys.*

         Commun. **2018**, 231, 140–145.

(56)   May, A. F.; Toberer, E. S.; Saramat, A.; Snyder, G. J. Characterization and analysis of

         thermoelectric transport in n-type $Ba_8Ga_{16-x}Ge_{30+x}$. *Phys. Rev. B* **2009**, *80*, 125205.

(57)   Zhao, L.-D.; Lo, S.-H.; He, J.; Li, H.; Biswas, K.; Androulakis, J.; Wu, C.-I.; Hogan, T.

         P.; Chung, D.-Y.; Dravid, V. P.; Kanatzidis, M. G. High performance thermoelectrics from

         earth-abundant materials: enhanced figure of merit in PbS by second phase nanostructures.

         J. Am. Chem. Soc. **2011**, *133*, 20476–20487.

(58)   Goto, Y.; Sakai, Y.; Kamihara, Y.; Matoba, M. Effect of Sn-Substitution on

         Thermoelectric Properties of Copper-Based Sulfide, Famatinite Cu_3SbS_4. *J. Phys. Soc. Jpn.*

         2015, *84*, 044706.

(59)   Kim, H. S.; Gibbs, Z. M.; Tang, Y.; Wang, H.; Snyder, G. J. Characterization of Lorenz

         number with Seebeck coefficient measurement. *APL Mater.* **2015**, *3*, 041506.

(60)   Toberer, E. S.; Zevalkink, A.; Snyder, G. J. Phonon Engineering through Crystal

Chemistry. *J. Mater. Chem.* **2011**, *21*, 15843–15852.

(61)   Gurunathan, R.; Hanus, R.; Snyder, G. J. Alloy scattering of phonons. *Mater. Horizons*

2020, *7*, 1452–1456.

(62)   Goto, Y.; Nishida, A.; Nishiate, H.; Murata, M.; Lee, C. H.; Miura, A.; Moriyoshi, C.;

Kuroiwa, Y.; Mizuguchi, Y. Effect of Te substitution on crystal structure and transport

properties of AgBiSe$_2$ thermoelectric material. *Dalt. Trans.* **2018**, *47*, 2575–2580.

(63)   Rowe, D. M.; Sjukla, V. S.; Savvides, N. *Nature* **1981**, *290*, 765–766.

(64)   Poudel, B.; Hao, Q.; Ma, Y.; Lan, Y.; Minnich, A.; Yu, B.; Yan, X.; Wang, D.; Muto, A.;

Vashaee, D.; Chen, X.; Liu, J.; Dresselhaus, M. S.; Chen, G.; Ren, Z. High-thermoelectric

performance of nanostructured bismuth antimony telluride bulk alloys. *Science* **2008**, *320*,

634–638.

(65)   Moshwan, R.; Yang, L.; Zou, J.; Chen, Z. G. Eco-friendly SnTe thermoelectric materials:

progress and future challenges *Adv. Funct. Mater.* **2017**, *27*, 30–44.

(66)   Zhang, W.; Chen, C.; Yao, H.; Xue, W.; Li, S.; Bai, F.; Huang, Y.; Li, X.; Lin, X.; Cao,

F.; Sui, J.; Wang, S.; Yu, B.; Wang, Y.; Liu, X.; Zhang, Q. Promising zintl-phase

thermoelectric compound SrAgSb. *Chem. Mater.* **2020**, *32*, 6983–6989.

(67)   Zevalkink, A.; Zeier, W. G.; Cheng, E.; Snyder, J.; Fleurial, J.-P.; Bux, S.

Nonstoichiometry in the Zintl Phase Yb$_{1-\delta}$Zn$_2$Sb$_2$ as a Route to Thermoelectric

Optimization. *Chem. Mater.* **2014**, *26*, 5710–5717.

(68)   Arguilla, M. Q.; Cultrara, N. D.; Baum, Z. J.; Jiang, S.; Ross, R. D.; Goldberger, J. E. EuSn$_2$As$_2$: an exfoliatable magnetic layered Zintl–Klemm phase. *Inorg. Chem. Front.* **2017**, *2*, 378–386.

(69)   Sakagami, R.; Goto, Y.; Karimata, H.; Azuma, N.; Yamaguchi, M.; Iwasaki, S.; Nakanishi, M.; Kitawaki, I.; Mizuguchi, Y.; Matoba, M.; Kamihara, Y. Thermoelectric transport properties of the van der Waals-type layered rhombohedral SnAs-based compound, EuSn$_2$As$_2$. *Jpn. J. Appl. Phys.* **2021**, *60*, 035511.

(70)   Themlin, J.-M.; Chtaïb, M.; Henrard, L.; Lambin, P.; Darville, J.; Gilles, J.-M. Characterization of tin oxides by x-ray-photoemission spectroscopy. *Phys. Rev. B* **1992**, *46*, 2460–2466.

(71)   Mori, H.; Usui, H.; Ochi. M.; Kuroki, K.; Temperature- and doping-dependent roles of valleys in the thermoelectric performance of SnSe: A first-principles study, *Phys. Rev. B* **2017**, 96, 085113.

(72)   Usui, H.; Suzuki, K.; Kuroki, K.; Nakano, S.; Kudo, K. Nohara, M.; Large Seebeck effect in electron-doped FeAs$_2$ driven by a quasi-one-dimensional pudding-mold-type band, *Phys. Rev. B* **2013**, 88, 075140.

(73)   Usui, H.; Shibata, S.; Kuroki, K.; Origin of coexisting large Seebeck coefficient and metallic conductivity in the electron doped SrTiO$_3$ and KTaO$_3$, *Phys. Rev. B* **2010**, 81, 205121.

(74)   Li, H.; Gao, S.; Duan, S.; Xu, Y.; Zhu, K. Dirac surface states in intrinsic magnetic topological insulators. *Phys. Rev. X* **2019**, *9*, 041039.

(75)   Gui, X.; Pletikosic, I.; Cao, H.; Tien, H. J.; Xu, X.; Zhong, R.; Wang, G.; Chang, T. R.; Jia, S.; Valla, T.; Xie, W.; Cava, R. J. A New Magnetic Topological Quantum Material Candidate by Design. *ACS Cent. Sci.* **2019**, *5*, 900–910.

Supporting Information for

Thermoelectric properties of the As/P-based Zintl compounds $EuIn_2As_{2-x}P_x$ ($x = 0$ to 2) and $SrSn_2As_2$

Keisuke Shinozaki,[1] Yosuke Goto,[1,*] Kazuhisa Hoshi,[1] Ryosuke Kiyama,[1] Naoto Nakamura,[1] Akira Miura,[2] Chikako Moriyoshi,[3] Yoshihiro Kuroiwa,[3] Hidetomo Usui,[4,*] Yoshikazu Mizuguchi[1]

[1]Department of Physics, Tokyo Metropolitan University, 1-1 Minami-osawa, Hachioji, Tokyo 192-0397, Japan

[2]Faculty of Engineering, Hokkaido University, Kita 13, Nishi 8 Sapporo 060-8628, Japan

[3]Graduate School of Advanced Science and Engineering, Hiroshima University, 1-3-1 Kagamiyama, Higashihiroshima, Hiroshima 739-8526, Japan

[4]Department of Physics and Materials Science, Shimane University, Matsue, 690-8504, Japan

e-mail: y_goto@tmu.ac.jp, hidetomo.usui@riko.shimane-u.ac.jp

Figure S1. Observed SXRD pattern of EuIn₂As₂₋ₓPₓ ($x = 0$, 0.6, and 1.0) and the Rietveld refinement results. The circles (red) and solid lines (black) represent the observed and calculated patterns, respectively. The difference between the observed and calculated patterns is shown at the bottom (blue). The vertical marks (green) indicate the Bragg reflection positions for EuIn₂As₂₋ₓPₓ, InAs, and In, respectively, from upper to lower. Amounts of impurity phases are denoted in the inset.
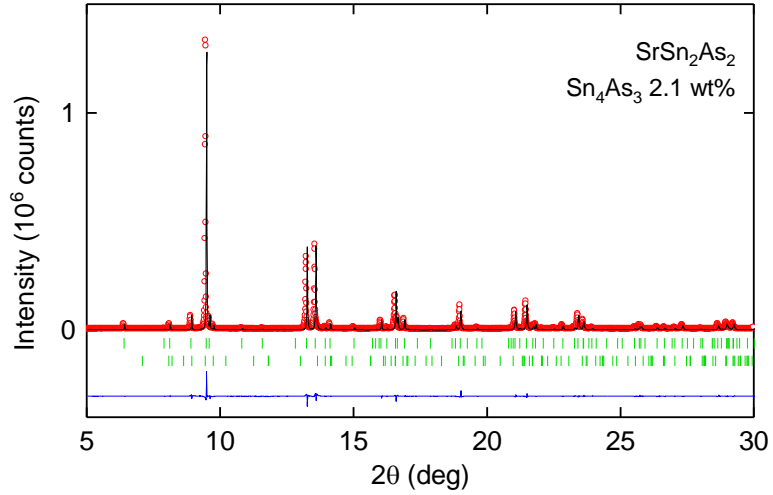
Figure S2. Observed SXRD pattern of SrSn$_2$As$_2$ and the Rietveld refinement results. The circles (red) and solid lines (black) represent the observed and calculated patterns, respectively. The difference between the observed and calculated patterns is shown at the bottom (blue). The vertical marks (green) indicate the Bragg reflection positions for SrSn$_2$As$_2$ and Sn$_4$As$_3$, respectively, from upper to lower. Amount of impurity phase are denoted in the inset.
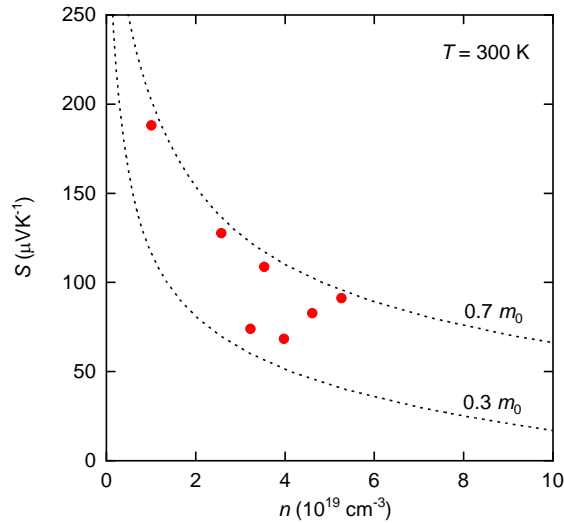
Figure S3. Seebeck coefficient as a function of carrier concentration for EuIn$_2$As$_{2-x}$P$_x$ at 300 K. The dashed lines are generated assuming a single parabolic band and acoustic-phonon scattering with density-of-states effective masses of 0.7 m_0 and 0.3 m_0, where m_0 is the rest mass of a free electron.
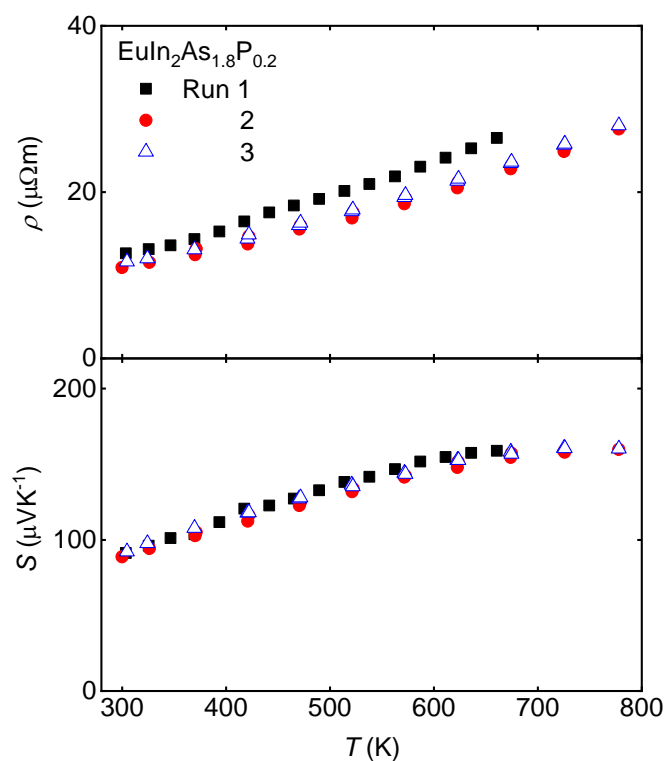
Figure S4. Repeated measurements of the electrical resistivity ρ and Seebeck coefficient S as a function of temperature T for $EuIn_2As_{1.8}P_{0.2}$.
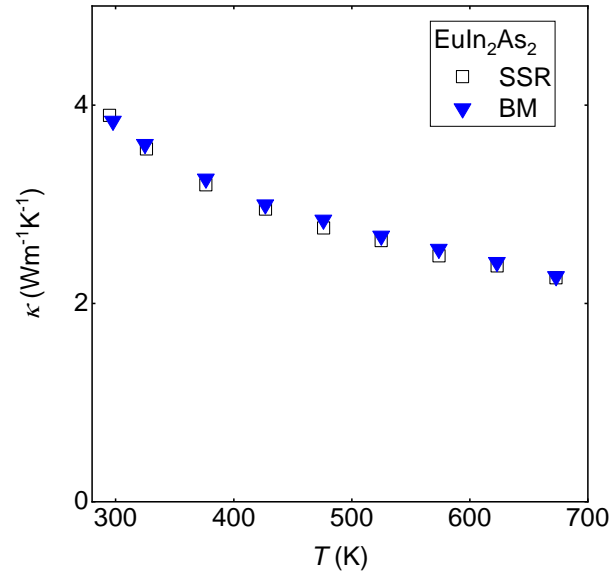
Figure S5. Powder XRD pattern of $EuIn_2As_2$ prepared by ball-milling followed by hot-pressing.
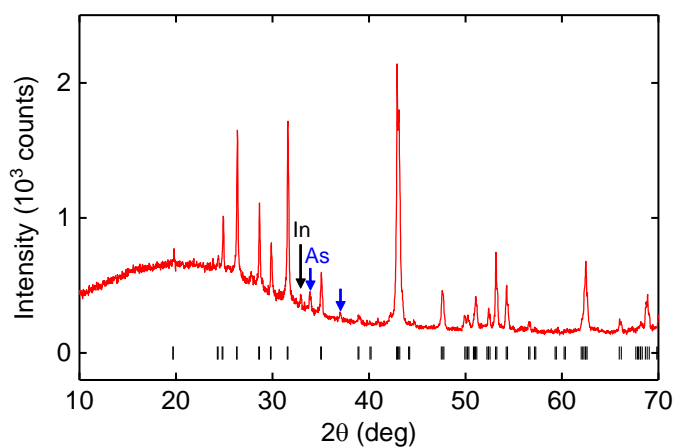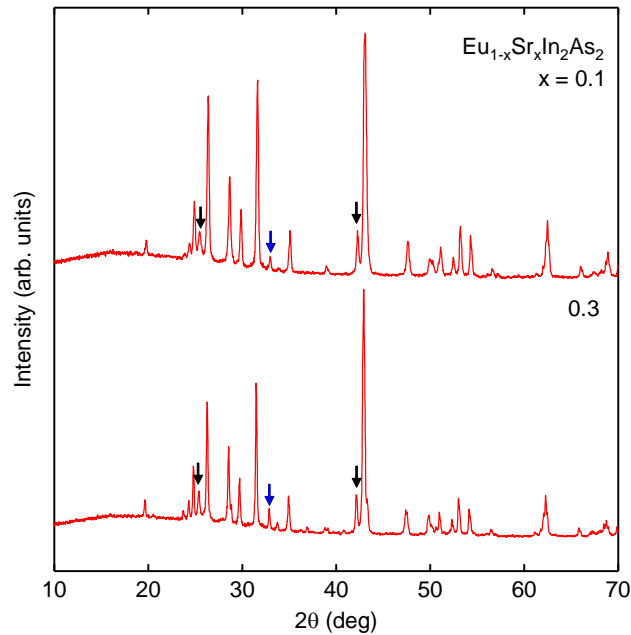

Arrows denote the diffraction peaks due to In (black) and As (blue) impurities.
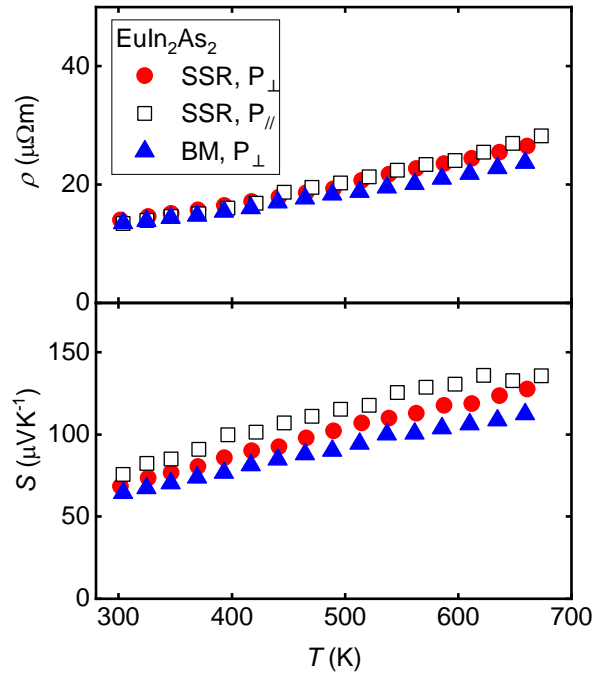
**Figure S6.** Temperature dependence of the electrical resistivity ρ and the Seebeck coefficient S for samples of $EuIn_2As_2$ prepared by using the solid-state reaction (SSR) method and by ball-milling followed by hot-pressing (BM). For the SSR sample, the results of measurements made parallel ($P_{//}$) or perpendicular ($P_{\perp}$) to the hot-pressing direction are also shown.
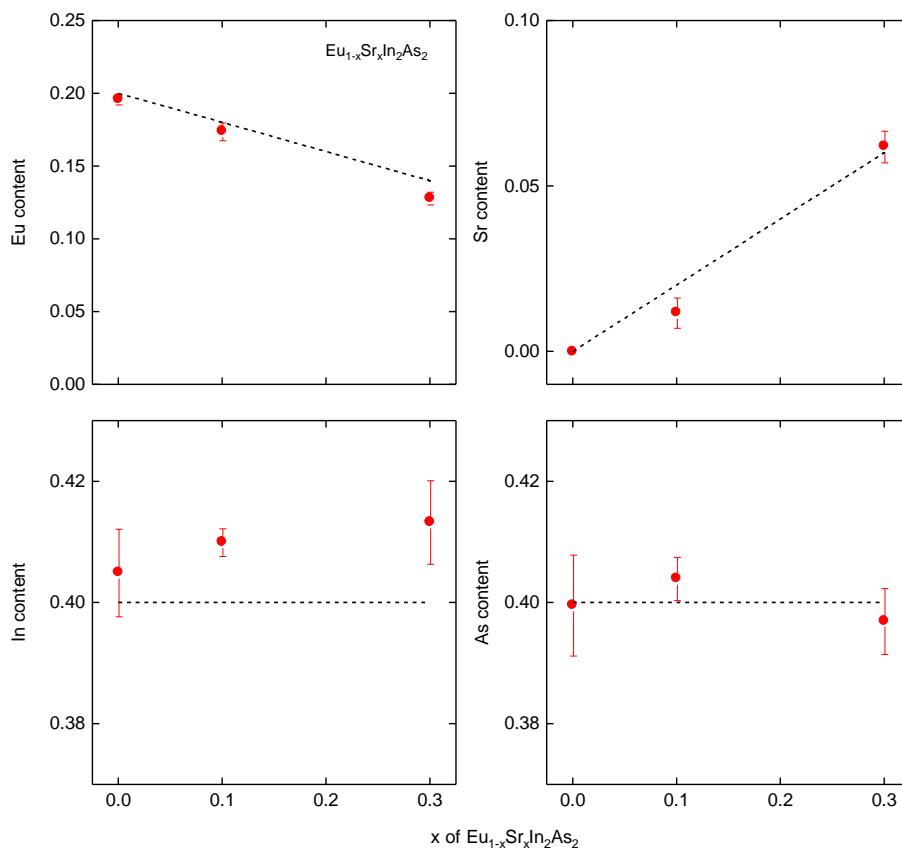
Figure S7. Temperature dependence of the thermal conductivity κ of EuIn$_2$As$_2$ prepared using the solid-state reaction (SSR) method and by ball-milling followed by hot-pressing (BM). For both samples, the measurements were made parallel to the hot-pressing direction.


Figure S8. XRD patterns of Eu$_{1-x}$Sr$_x$In$_2$As$_2$ ($x = 0.1$ and 0.3). Arrows denote the diffraction peaks due to InAs (black) and In (blue) impurities.
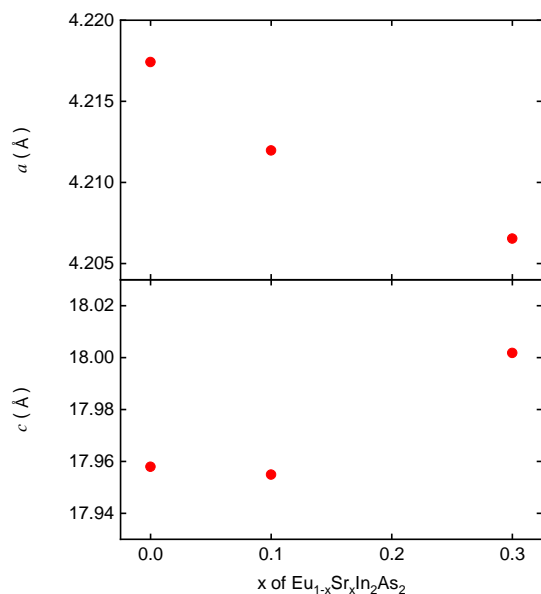
**Figure S9.** Lattice parameters of $Eu_{1-x}Sr_xIn_2As_2$. Error bars are smaller than the symbols.

Figure S10. Chemical compositions of $Eu_{1-x}Sr_xIn_2As_2$ obtained using EDX. The dashed lines represent the nominal compositions of the starting materials.
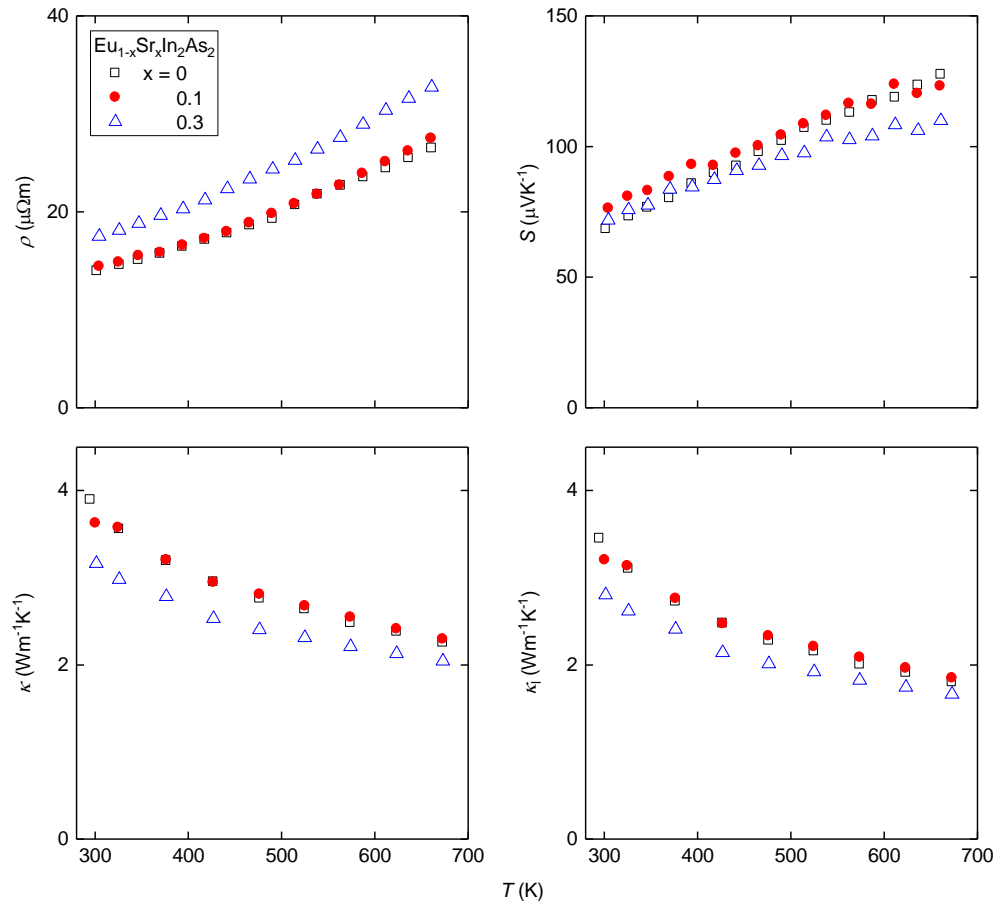
Figure S11. Temperature dependence of the electrical resistivity ρ, the Seebeck coefficient S, the total thermal conductivity κ, and the lattice thermal conductivity κ_l of $Eu_{1-x}Sr_xIn_2As_2$.
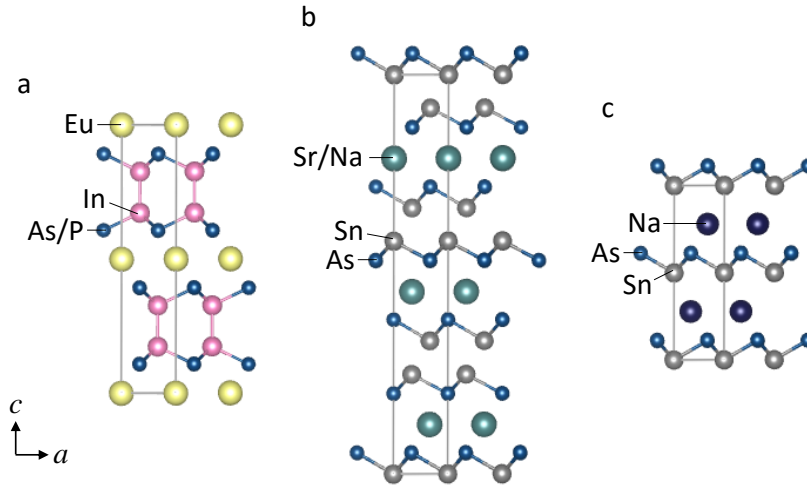
Figure S12. Schematic illustrations of the crystal structures of (a) $EuIn_2As_{2-x}P_x$ (space group $P6_3/mmc$) and (b) $Sr(Na)Sn_2As_2$ (space group $R\bar{3}m$), and (c) NaSnAs (space group $P6_3mc$)). The outlined regions represent the unit cells.
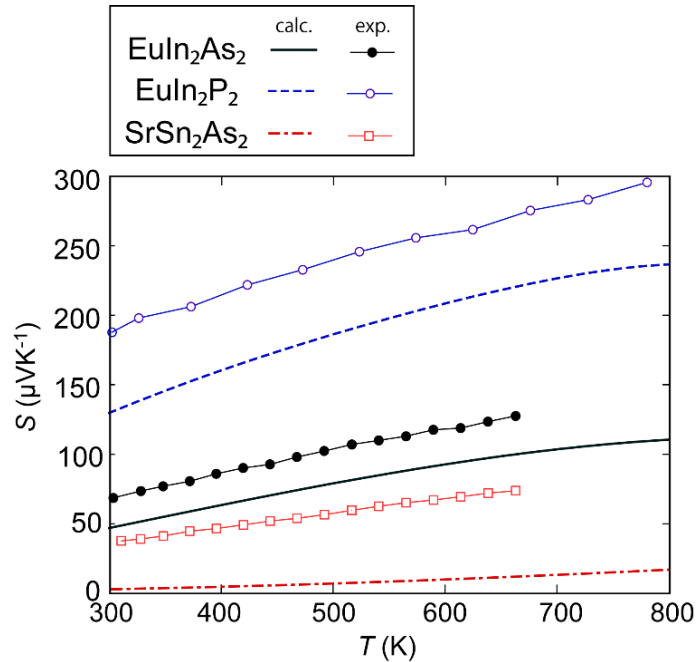
Figure S13. Temperature dependence of the experimentally and theoretically determined Seebeck coefficients. To calculate the Seebeck coefficient, we fixed the hole concentrations of $EuIn_2As_2$, $EuIn_2P_2$, and $SrSn_2As_2$ to be 4.0×10^{19} cm^{-3}, 1.0×10^{19} cm^{-3}, and 1.6×10^{21} cm^{-3}, respectively.